

## Article

# A Novel UAV Air-to-Air Channel Model Incorporating the Effect of UAV Vibrations and Diffuse Scattering

Wenzhe Qi <sup>1,†</sup>, Ji Bian <sup>2,3,\*</sup>, Zili Wang <sup>2,3</sup> and Wenzhao Liu <sup>1</sup>

<sup>1</sup> State Grid Shandong Electric Power Company Zibo Power Supply Company, Zibo 255000, China; qiwenzhe67@163.com (W.Q.); towwwwlwz19831205@sina.com (W.L.)

<sup>2</sup> School of Information Science and Engineering, Shandong Normal University, Jinan 250358, China; wzili22@163.com

<sup>3</sup> Key Laboratory of New Technology for Distributed Computer Software of Shandong Province, Shandong Normal University, Jinan 250358, China

\* Correspondence: jibian@sdu.edu.cn

† These authors contributed equally to this work.

**Abstract:** In this paper, we propose a geometric channel model for air-to-air (A2A) unmanned aerial vehicle (UAV) communication scenarios. The model is established by incorporating line-of-sight, specular reflection, and diffuse scattering components, and it can capture the impacts of UAV vibrations induced by the propeller's rotation. Based on UAV heights and ground scatterer density, a closed-form expression is derived to jointly capture the zenith and azimuth angular distributions of diffuse rays. The power of diffuse rays is modeled according to the grazing angle of the rays and the electrical properties and roughness of the ground materials. Key statistics, including the temporal autocorrelation function, spatial cross-correlation function, Doppler power spectrum density, and coherence time are derived, providing an in-depth understanding of the time-variant characteristics of the channel. The results indicate that the presented model is capable of capturing certain A2A channel characteristics, which align with the corresponding theoretical analysis. The findings suggest that the scattering effect of the A2A channel is significantly influenced by the altitude of the UAV. Additionally, it is shown that UAV vibrations can introduce extra Doppler frequencies, notably decreasing the temporal correlation and coherence time of the channel. This effect is more prominent when the system operates at high-frequency bands. The effectiveness of the presented model is confirmed through a comparison of its statistics with those of an existing model and with available measurement data.

**Keywords:** UAV channels; UAV vibrations; A2A channels; channel models; channel statistics



**Citation:** Qi, W.; Bian, J.; Wang, Z.; Liu, W. A Novel UAV Air-to-Air Channel Model Incorporating the Effect of UAV Vibrations and Diffuse Scattering. *Drones* **2024**, *8*, 194. <https://doi.org/10.3390/drones8050194>

Academic Editor: Carlos Tavares Calafate

Received: 5 April 2024  
Revised: 8 May 2024  
Accepted: 10 May 2024  
Published: 12 May 2024



**Copyright:** © 2024 by the authors. Licensee MDPI, Basel, Switzerland. This article is an open access article distributed under the terms and conditions of the Creative Commons Attribution (CC BY) license (<https://creativecommons.org/licenses/by/4.0/>).

## 1. Introduction

Unmanned aerial vehicles (UAVs) are cost-effective and highly mobile, making them promising alternatives to conventional ground facilities in the development of future wireless communication systems [1]. UAVs can serve as aerial access points to extend service areas or act as relay nodes to establish intelligent flying ad hoc networks [2]. Given their crucial role in the design of UAV communications, creating practical and efficient channel models for UAV communication has become an urgent requirement.

### 1.1. Related Works

At present, studies on UAV channel modeling primarily concentrate on air-to-ground (A2G) situations. For instance, Chang et al. introduced an A2G model, where the scattering region is defined as the intersecting section of the ground and an ellipsoid with focal points at the UAV and ground station [3]. The authors further presented a more generalized model by developing a 3GPP-like cluster-based A2G model [4], where the term “cluster” refers to multipath components (MPCs) sharing comparable delays and angles. In [5],

A2G channel measurements were performed at 3.5 GHz within a campus environment. The results indicate the A2G channels consist of line-of-sight (LoS), ground reflection, and MPCs originating from ground scatterers. Variations over time in channel characteristics, such as path loss and MPC angles, were observed due to UAV flights. In addition, various studies have explored the dynamic movement of UAVs. For example, Lian et al. proposed an A2G model that relaxed the linear trajectory condition of the UAV [6]. Specifically, the UAV was allowed to move with constant acceleration and angular speed. Bian et al. reported a more practical model, which was devised by integrating a geometric model with the smooth-turn mobility model [7]. The latter was employed to generate UAV trajectories that accurately capture the aerodynamics of UAVs.

In addition to exploring dynamic trajectories, several A2G channel models have been specifically crafted to account for the effects of UAV self-rotation [8,9]. For instance, Bai et al. proposed an A2G model that incorporated the UAV self-rotation effect using a rotation matrix [8]. This matrix updated the local coordinates of antennas after a three-dimensional (3D) rotation of the UAV. Hua et al. adopted a comparable method, simulating the posture variation of the UAV [9]. The influences of UAV posture variation on channel behavior were investigated. However, it is worth noting that the rotation angles in these two models were represented as constant or linearly varying values, oversimplifying the depiction of UAV dynamics [8,9]. A more realistic model was given by Ma et al., where the pitch angle of the UAV was represented by a deterministic sinusoidal process, indicating that the amplitude and frequency of the pitch angle variations remain constant over time [10]. Furthermore, considering the impact of wind gusts, Banagar et al. described the random wobbling of the UAV using a stochastic sinusoidal process [11]. To mitigate computational complexity, this model merely considered the pitch angle of the UAV platform, limiting the vibrations to the vertical plane. In addition to the aforementioned approaches, Dabiri et al. conducted an evaluation of UAV millimeter-wave links, where UAVs were equipped with planar arrays [12]. The boresight direction of the array was assumed to follow a Gaussian distribution. The impact of antenna misalignment loss on system performance was analyzed. Additionally, a more intricate model was presented by Ma et al., where the roll and pitch rotations of the UAV were modeled using a Gauss–Markov model [13]. It is essential to note that both the Gauss and Gauss–Markov wobbling models have not yet been validated through measurements. In general, the aforementioned models primarily focus on the rotation of the UAV, indicating that the UAVs undergo a turning or rotational motion [8–13]. The UAV rotation may be relevant for reflecting the influence of atmospheric turbulence and wind gusts. However, when considering the operations of propellers and engines, both the UAV and antennas may experience high-frequency repetitive movements [14]. This refers to oscillating or back-and-forth motions around an equilibrium position, rather than spinning motions. Measurements indicate that the rotation of UAV propellers generates distinct Doppler frequency shift patterns in radar returns, markedly different from the Doppler characteristics of slow-moving scatterers like trees and birds. In [15], a technique for UAV detection and tracking was proposed utilizing micro-Doppler signatures from a multistatic radar system. The results demonstrated that micro-Doppler features are effective in distinguishing UAVs from clutter, especially when the UAV is hovering or moving with low radial velocities. Note that the authors focused on UAV detection and tracking, rather than channel modeling.

Regarding the propagation scenario, the existing literature predominantly focuses on A2G scenarios in UAV channel modeling. However, only a limited number of UAV channel models are suitable for air-to-air (A2A) scenarios, with most of them emphasizing the larger-scale fading of the A2A link. Liu et al. conducted a preliminary measurement for A2A communications [16]. Their findings revealed a decrease in both multipath and shadowing fading as the UAV altitude increases. Furthermore, they introduced a modified log-distance path-loss model. Similar investigations were undertaken by Ede et al. and Zhou et al., who estimated path-loss exponents and proposed path-loss models for A2A communications based on measurement and ray-tracing results [17,18]. In general, A2A

channel modeling on small-scale fading is still in its early stages, with most studies relying on classical geometric models such as the ellipsoid model [19], two-sphere model [20], and cylinder model [21].

Furthermore, when a wave encounters rough surfaces or small objects relative to wavelength, the incident wave is split into a specular ray, which follows Snell's Law, and multiple diffuse rays that scatter in various directions [22]. The proportion of diffuse components in the received power is determined by the grazing angle of the wave, the roughness of the surface, and the electrical properties of reflective materials. Measurements conducted at 1.35 GHz in an industrial scenario indicated that the diffuse components account for 15–80% of the channel power [23]. Similarly, measurements conducted at 5.2 GHz revealed that the proportion of diffuse component power in the total received power can achieve a maximum of 90% in urban non-LoS (NLoS) scenarios [24]. In UAV communications, large altitudes of the UAV result in large grazing angles. This means a large amount of energy can be scattered instead of reflected. However, the above-mentioned UAV models were obtained by summing discrete multipath components originating from large discrete objects, and the contribution of the diffuse components was neglected, which may lead to an underestimation of the received power and channel capacity [25].

With the proliferation of mobile devices, expansive bandwidths, diverse system configurations, and varied propagation environments, there is a growing inclination toward integrating machine learning techniques into UAV communication systems. In [26], an A2G channel model was presented by introducing a generative adversarial network (GAN) into a traditional geometry-based model, where the GAN was used to generate the angle offsets within the clusters. A generative neural network for A2G channel generation was proposed in [27]. Specifically, the LoS/NLoS state was first predicted and then fed into a conditional variational autoencoder (VAE) to generate the channel parameters, including the path loss, delay, and angles of MPCs. Similarly, in [28], an A2G channel generation method was proposed using a conditional GAN. The channel parameters, including the gain, delay, and angles of MPCs, were randomly generated based on the UAV's location and speed. A radio environment map (REM) provides a comprehensive representation of radio frequency information across various propagation environments. In [29], a scenario-dependent channel dictionary that incorporates specific channel properties was initially constructed. Subsequently, an REM was developed using a sparse Bayesian learning algorithm. In [30], a UAV-based federated learning scheme was introduced. In addition to covert model parameter uploading, the UAV also transmits artificial noise to unintended users, thereby reducing the likelihood of information eavesdropping. Furthermore, a distributed proximal policy optimization was employed to achieve a tradeoff between security and training costs. Similarly, in [31], a secure federated learning framework was presented, which utilizes a blockchain-based architecture for securing data training and validating contributions among UAVs.

## 1.2. Motivations

Channel models are essential for the development and performance analysis of UAV communication systems. However, the majority of existing channel models concentrate on terrestrial or A2G scenarios, and studies focusing on A2A scenarios are scarce. In traditional terrestrial communications, the heights of the transmitter (Tx) and receiver (Rx) are typically small compared to the distance between them. The small grazing angles lead to a significant amount of energy being reflected by the ground. Hence, the amplitude of the reflection coefficient is approximated to one, and the phase shift between the direct and ground reflection paths is close to  $180^\circ$ , known as perfect ground reflection [32]. However, in A2A scenarios, UAVs have the ability to hover at high altitudes. The large grazing angles lead to a significant portion of the signal energy being scattered rather than reflected. Hence, it is essential to accurately model the diffuse scattering components in the A2A channel. Additionally, in A2A scenarios, both the Tx and Rx are relatively high, resulting in a different distribution of the scatterers compared to A2G scenarios [33]. Hence, existing

A2G models are not applicable to A2A scenarios. Moreover, although some existing models primarily focus on the vibration effects on UAVs, in these scenarios, UAVs undergo turning or rotational motions, which are caused by wind gusts or atmospheric turbulence [10–13]. However, when considering the operation of propellers and engines, the UAV can undergo frequent repetitive movements, involving oscillating or back-and-forth motions around an equilibrium position [14,34]. Unlike A2G channels, A2A channels undergo dual vibrations at both ends of the link. The statistical features of A2A channels, incorporating vibrations from UAVs at both ends of the link and considering LoS, specular, and diffuse components, have not been adequately investigated.

### 1.3. Contributions

Considering the aforementioned research limitations, this paper presents a novel model for A2A communication scenarios, which aims to capture the channel characteristics that impact the statistics of A2A channels. The model is composed of the LoS, specular reflection, and diffuse components of the channel, effectively representing the influences of UAV vibrations on channel properties. Important statistics such as the spatial-temporal cross-correlation function (CCF), Doppler power spectrum density (PSD), and coherence time are derived. The key contributions include the following:

- A novel A2A channel model combining LoS, specular reflection, and diffuse components is proposed. The channel properties are characterized in the presence of large-scale path loss and small-scale fading. Additionally, the proposed model can capture the effects of both large-scale and small-scale mobilities of UAVs. The former refers to UAVs' flight, while the latter describes UAVs' random vibrations caused by propeller rotation and engine operation at both ends of the link.
- We derive a closed-form expression that jointly describes the zenith and azimuth angles of diffuse rays as the function of the UAV's location and the dispersion of scatterers. The power of the diffuse rays is calculated by taking into account various factors, such as the path loss, reflection coefficient, and scattering radiation pattern. This is determined based on the grazing angles of impinging rays and the electrical properties and roughness of the reflective materials.
- Key statistics incorporating the spatial-temporal CCF, Doppler PSD, and coherence time are derived. The impacts of model parameters on channel statistics are presented, including the UAV's altitude and the scattering lobe width, as well as the amplitude, direction, and frequency of UAV vibration. We show that the random vibration of UAVs can reduce the temporal correlation and coherence time of the channel and induce extra Doppler frequency components. The influences of UAV vibrations become more pronounced as the carrier frequency increases.

The rest of this paper is structured as follows. Section 2 outlines the channel model for A2A communication scenarios. A statistical analysis is conducted in Section 3. Section 4 presents the findings and discussion, while Section 5 draws the conclusions.

## 2. The 3D A2A MIMO Channel Model

Figure 1 illustrates a typical A2A communication scenario, which includes an LoS ray, a specular reflection ray following Snell's Law, and multiple diffuse rays [2]. Without loss of generality, the projection of the Tx array center onto the  $xy$  plane is chosen as the origin of coordinates, denoted by  $O$ . The horizontal separation between the centers of the Tx and Rx arrays is denoted as  $D$ . The Tx (Rx) flies horizontally at an altitude  $h_t$  ( $h_r$ ) with a speed  $v_t$  ( $v_r$ ) and follows a specific moving direction denoted as  $\alpha_t$  ( $\alpha_r$ ). Both the Tx and Rx employ uniform linear arrays comprising  $P$  and  $Q$  antennas, which are spaced at distances  $\delta_t$  and  $\delta_r$ , respectively. Angles  $\zeta_t$  and  $\zeta_r$  define the Tx and Rx arrays' orientations in the horizontal plane, respectively.

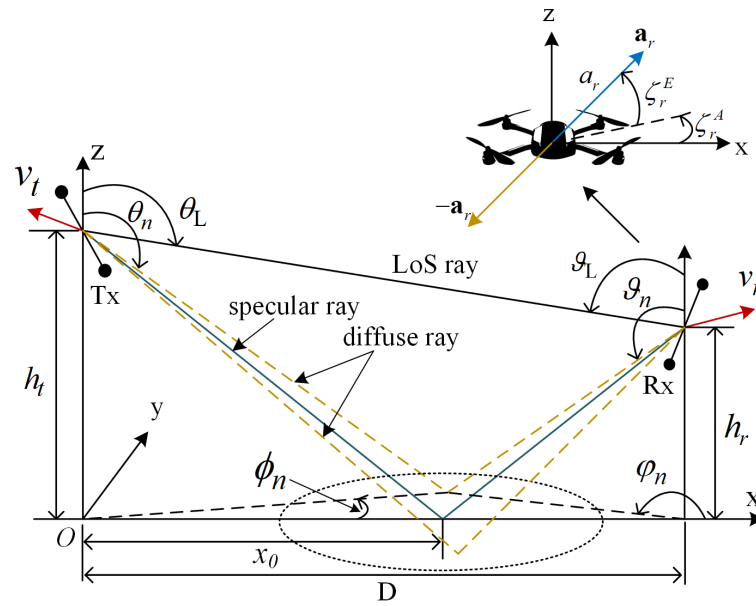


Figure 1. The geometrical characteristics of the proposed A2A MIMO channel model.

Owing to propeller rotation, UAVs often exhibit sinusoidal vibrations, which are particularly relevant in the study of small UAVs [14,34]. These periodic motions of UAVs can be characterized by the displacement varying over time and are modeled as

$$\mathbf{x}_t(t) = \mathbf{a}_t \cdot \sin(2\pi f_t \cdot t + \Theta_t) \tag{1}$$

$$\mathbf{x}_r(t) = \mathbf{a}_r \cdot \sin(2\pi f_r \cdot t + \Theta_r). \tag{2}$$

Here,  $f_t$  and  $f_r$  are the vibration frequencies of the Tx and Rx antennas, respectively;  $\Theta_t$  and  $\Theta_r$  are the initial phases, which follow uniform distributions within  $[0, 2\pi)$ ; and  $\mathbf{a}_t$  and  $\mathbf{a}_r$  are vibrational displacement amplitude vectors, which are expressed as

$$\mathbf{a}_t = a_t [\cos \zeta_t^E \cos \zeta_t^A, \cos \zeta_t^E \sin \zeta_t^A, \sin \zeta_t^E]^T \tag{3}$$

$$\mathbf{a}_r = a_r [\cos \zeta_r^E \cos \zeta_r^A, \cos \zeta_r^E \sin \zeta_r^A, \sin \zeta_r^E]^T \tag{4}$$

where  $(\cdot)^T$  denotes the matrix transpose,  $a_t$  and  $a_r$  are vibrational displacement amplitudes following uniform distributions, and  $\zeta_t^E$  and  $\zeta_t^A$  are the vibration elevation and azimuth angles of the transmit UAV, respectively. Similarly,  $\zeta_r^E$  and  $\zeta_r^A$  are the vibration elevation and azimuth angles of the receiving UAV, respectively. Note that (1) and (2) describe a rapid oscillating or back-and-forth motion of the UAV rather than a rotation. This is different from existing models in which the UAVs undergo rotational motions [10–13].

The multiple-input multiple-output (MIMO) channel matrix  $\mathbf{h}(t, \tau) = [h_{qp}(t, \tau)]_{Q \times P}$  can be obtained as

$$\mathbf{h}(t, \tau) = \mathbf{h}_{\text{LoS}}(t, \tau) + \mathbf{h}_{\text{NLoS}}(t, \tau) \tag{5}$$

where  $\mathbf{h}_{\text{LoS}}(t, \tau)$  and  $\mathbf{h}_{\text{NLoS}}(t, \tau)$  are the channel matrices for the LoS and NLoS components of the channel, respectively. Additionally,  $h_{qp}(t, \tau)$  denotes the time-varying channel impulse response (CIR) between  $A_p^t$  and  $A_q^r$ , where  $A_p^t$  denotes the  $p$ th Tx antenna and  $A_q^r$  accounts for the  $q$ th Rx antenna. For clarity, the essential parameters of the model are summarized in Table 1.

**Table 1.** Summary of key parameter definitions.

Parameter	Definition
$O$	The origin of coordinates
$P, Q$	Numbers of Tx and Rx antennas, respectively
$A_p^t, A_q^r$	The $p$ th Tx and the $q$ th Rx antennas, respectively
$\xi_t, \xi_r$	Tilt angles of Tx and Rx arrays in the horizontal plane, respectively
$\delta_t, \delta_r$	Spacings between adjacent antennas at the Tx and Rx arrays, respectively
$h_t, h_r$	Heights of the Tx and Rx, respectively
$D$	Horizontal separation between Tx and Rx centers
$x_0$	Distance from $O$ to the specular reflection point
$\theta_n, \vartheta_n, \phi_n, \varphi_n$	ZoD, ZoA, AoD, and AoA of the $n$ th ray
$\theta_{i,n}$	Incident angle of the $n$ th ray
$d_L, d_n$	Lengths of the LoS and the $n$ th ray, respectively
$v_t, v_r$	Speeds of the Tx and Rx, respectively
$\alpha_t, \alpha_r$	Angles of motion of the Tx and Rx, respectively
$\mathbf{a}_t, \mathbf{a}_r$	Vibration displacement vectors of the Tx and Rx antennas, respectively
$f_t, f_r$	Vibration frequencies of the Tx and Rx antennas, respectively
$a_t, a_r$	Vibration amplitudes of the Tx and Rx antennas, respectively
$\zeta_{t(r)}^E, \zeta_{t(r)}^A$	Vibration elevation and azimuth angles of the Tx and Rx antennas, respectively

### 2.1. LoS Component

The channel matrix for the LoS component is written as

$$\mathbf{h}_{\text{LoS}}(t, \tau) = \mathbf{v}_r(\vartheta_L, \varphi_L) \mathbf{v}_t^H(\theta_L, \phi_L) \cdot \sqrt{P_L} \cdot e^{-j\frac{2\pi}{\lambda} d_L(t)} \cdot \delta(\tau - \tau_L(t)) \quad (6)$$

where  $(\cdot)^H$  denotes the conjugate transpose,  $\lambda = c/f_c$  denotes the wavelength,  $c$  accounts for the speed of light, and  $f_c$  denotes the carrier frequency. In (6), the transmit and receive array steering vectors are given as

$$\mathbf{v}_t(\theta_L, \phi_L) = [1, e^{-j\frac{2\pi}{\lambda} \delta_t \sin \theta_L \cos(\phi_L - \xi_t)}, \dots, e^{-j\frac{2\pi}{\lambda} (P-1) \delta_t \sin \theta_L \cos(\phi_L - \xi_t)}]^T \quad (7)$$

$$\mathbf{v}_r(\vartheta_L, \varphi_L) = [1, e^{-j\frac{2\pi}{\lambda} \delta_r \sin \vartheta_L \cos(\varphi_L - \xi_r)}, \dots, e^{-j\frac{2\pi}{\lambda} (Q-1) \delta_r \sin \vartheta_L \cos(\varphi_L - \xi_r)}]^T \quad (8)$$

where  $\theta_L$  is the zenith angle of departure (ZoD—the departure angle relative to the  $+z$  axis), i.e.,

$$\theta_L = \frac{\pi}{2} + \arctan\left(\frac{h_t - h_r}{D}\right). \quad (9)$$

The parameter  $\vartheta_L$  is the zenith angle of arrival (ZoA) and is calculated as  $\vartheta_L = \pi - \theta_L$ . The azimuth angle of departure (AoD) and azimuth angle of arrival (AoA) are  $\phi_L = 0$  and  $\varphi_L = \pi$ , respectively. Due to the large Tx–Rx distance, it is considered that the angles remain unchanged over the small observation time interval. The delay of the LoS path is  $\tau_L(t) = d_L(t)/c$ .

**Proposition 1.** *The time-varying travel distance of the LoS ray incorporating the effects of UAV movements and antenna vibrations can be calculated as*

$$d_L(t) \approx d_L + v_r t \sin \vartheta_L \cos \alpha_r - v_t t \sin \theta_L \cos \alpha_t + a_r \sin(2\pi f_r t) \cos(\gamma_r^L) - a_t \sin(2\pi f_t t) \cos(\gamma_t^L) \quad (10)$$

where  $d_L$  is the length of the LoS path at the initial time and is calculated as

$$d_L = \sqrt{(h_t - h_r)^2 + D^2}. \tag{11}$$

Additionally,  $\gamma_t^L$  is the angle between  $\mathbf{a}_t$  and the LoS ray and is determined as

$$\cos(\gamma_t^L) = \frac{\mathbf{a}_t^T \Phi_L}{|\mathbf{a}_t| \cdot |\Phi_L|} \tag{12}$$

where  $\Phi_L$  is the departure angle unit vector of the LoS ray, i.e.,

$$\Phi_L = \begin{bmatrix} \sin \theta_L \cos \phi_L \\ \sin \theta_L \sin \phi_L \\ \cos \theta_L \end{bmatrix}. \tag{13}$$

Similarly,  $\gamma_r^L$  is the angle between  $\mathbf{a}_r$  and the LoS ray and is determined as

$$\cos(\gamma_r^L) = \frac{\mathbf{a}_r^T \Phi_L}{|\mathbf{a}_r| \cdot |\Phi_L|}. \tag{14}$$

**Proof of Proposition 1.** Owing to the UAV's movement, the mean distance from the Tx to Rx at time  $t$  can be expressed as

$$\bar{d}_L(t) = |\mathbf{d}_L + \mathbf{m}_r t - \mathbf{m}_t t| \tag{15}$$

where  $\mathbf{d}_L = d_L \Phi_L$  is the vector from the Tx to the Rx at the initial time instant, and  $\mathbf{m}_t = v_t [\cos \alpha_t, \sin \alpha_t, 0]^T$  and  $\mathbf{m}_r = v_r [\cos \alpha_r, \sin \alpha_r, 0]^T$  are the velocity vectors of the Tx and Rx, respectively. Considering the short observation time interval,  $\bar{d}_L(t)$  can be calculated as [35]

$$\bar{d}_L(t) \approx d_L + v_r t \sin \theta_L \cos \alpha_r - v_t t \sin \theta_L \cos \alpha_t. \tag{16}$$

The time-varying distance between the Tx and the Rx, considering the transmit UAV's vibration, is obtained as

$$d'_L(t) = |\bar{\mathbf{d}}_L(t) - \mathbf{x}_t(t)| \\ = \sqrt{\bar{d}_L(t)^2 + |\mathbf{x}_t(t)|^2 - 2\bar{d}_L(t)|\mathbf{x}_t(t)| \cos(\gamma_t^L)} \tag{17}$$

where  $\bar{\mathbf{d}}_L(t) = \bar{d}_L(t) \Phi_L$ . Note that  $a_t \ll \bar{d}_L(t)$ . Using the approximation  $\sqrt{1-x} \approx 1 - \frac{x}{2}$  for small  $x$ , and substituting (16) into (17), we have

$$d'_L(t) \approx d_L + v_r t \sin \theta_L \cos \alpha_r - v_t t \sin \theta_L \cos \alpha_t - a_t \sin(2\pi f_t t) \cos(\gamma_t^L). \tag{18}$$

Equation (10) can be derived by applying a similar procedure that takes both the transmit and receiving UAVs' vibrations into account.  $\square$

By substituting (7), (8), and (10) into (6), the CIR of the LoS component between  $A_p^t$  and  $A_q^r$  can be expressed as

$$h_{qp}^{\text{LoS}}(t, \tau) = \sqrt{P_L} \cdot e^{-j\frac{2\pi}{\lambda} d_L} \cdot e^{j\frac{2\pi}{\lambda} (p-1)\delta_t \sin \theta_L \cos(\phi_L - \xi_t)} \cdot e^{-j\frac{2\pi}{\lambda} (q-1)\delta_r \sin \theta_L \cos(\phi_L - \xi_r)} \\ \times e^{j2\pi(v_t^t + v_r^t)t} \cdot e^{j\frac{2\pi}{\lambda} a_t \sin(2\pi f_t t) \cos(\gamma_t^L)} \cdot e^{-j\frac{2\pi}{\lambda} a_r \sin(2\pi f_r t) \cos(\gamma_r^L)} \cdot \delta(\tau - \tau_L(t)) \tag{19}$$

where  $v_t^L$  and  $v_r^L$  are the Doppler shifts at the Tx and Rx sides, respectively, which are given as

$$v_t^L = \frac{v_t}{\lambda} \sin \theta_L \cos \alpha_t \quad (20)$$

$$v_r^L = -\frac{v_r}{\lambda} \sin \theta_L \cos \alpha_r. \quad (21)$$

Equation (19) yields insight into the phase variation in the A2A channel. Specifically, the phase of the channel is decomposed into the following components:

- $-\frac{2\pi}{\lambda} d_L$  accounts for the phase shift due to the initial propagation distance  $d_L$ .
- $\frac{2\pi}{\lambda} (p-1) \delta_t \sin \theta_L \cos(\phi_L - \xi_t)$  is the phase shift due to the relative locations of  $A_p^t$  in the Tx array.
- $-\frac{2\pi}{\lambda} (q-1) \delta_r \sin \theta_L \cos(\phi_L - \xi_r)$  is the phase shift due to the relative locations of  $A_q^r$  in the Rx array.
- $2\pi(v_t^L + v_r^L)t$  is the phase shift due to the large-scale movements of the UAVs in specific directions.
- $\frac{2\pi}{\lambda} a_t \sin(2\pi f_t t) \cos(\gamma_t^L)$  is the phase shift stemming from the random vibration of the Tx antennas
- $-\frac{2\pi}{\lambda} a_r \sin(2\pi f_r t) \cos(\gamma_r^L)$  is the phase shift due to the random vibrations of the Rx antennas.

We define the phase rotation stemming from the antenna vibrations as follows:

$$\theta_{\text{wob}}(t) = \frac{2\pi}{\lambda} [a_t \sin(2\pi f_t t) \cos(\gamma_t^L) - a_r \sin(2\pi f_r t) \cos(\gamma_r^L)]. \quad (22)$$

The antenna vibrations introduce an effective time-varying Doppler frequency, i.e.,

$$\begin{aligned} \nu_{\text{wob}}(t) &= \frac{1}{2\pi} \frac{d\theta_{\text{wob}}(t)}{dt} \\ &= \frac{2\pi}{\lambda} [f_t a_t \cos(2\pi f_t t) \cos(\gamma_t^L) - f_r a_r \cos(2\pi f_r t) \cos(\gamma_r^L)]. \end{aligned} \quad (23)$$

It is clear that the value of  $\nu_{\text{wob}}(t)$  depends on the vibration's amplitude, frequency, and direction, while the vibration frequency governs its temporal variation, which follows cosine functions. To further illustrate this, we employ the Jacobi–Anger expansion, i.e.,

$$e^{iz \sin \theta} = \sum_{n=-\infty}^{\infty} J_n(z) e^{in\theta} \quad (24)$$

where  $J_n(\cdot)$  is the  $n$ th-order Bessel function of the first kind [36], and (19) can be expanded as follows:

$$\begin{aligned} &h_{qp}^{\text{LoS}}(t, \tau) \\ &= \sqrt{P_L} \cdot e^{-j\frac{2\pi}{\lambda} d_L} \cdot e^{j\frac{2\pi}{\lambda} (p-1) \delta_t \sin \theta_L \cos(\phi_L - \xi_t)} \cdot e^{-j\frac{2\pi}{\lambda} (q-1) \delta_r \sin \theta_L \cos(\phi_L - \xi_r)} \cdot e^{j2\pi(v_t^L + v_r^L)t} \\ &\times \sum_{n_1=-\infty}^{+\infty} \sum_{n_2=-\infty}^{+\infty} \left\{ J_{n_1} \left( \frac{2\pi}{\lambda} a_t \cos \gamma_t^L \right) \cdot J_{n_2} \left( -\frac{2\pi}{\lambda} a_r \cos \gamma_r^L \right) e^{j(n_1 f_t + n_2 f_r)t} \right\} \cdot \delta(\tau - \tau_L(t)). \end{aligned} \quad (25)$$

This expression indicates that the antenna vibration introduces a series of sidebands at frequency offsets  $k_1 f_t + k_2 f_r$ . The PSDs of the LoS path with different carrier frequencies are shown in Figure 2. To facilitate the analysis, we set  $v_t = v_r = 0$  m/s,  $f_t = f_r = 20$  Hz, and the antennas vibrate with a fixed amplitude, i.e.,  $a_t = a_r = 0.01$  m. In accordance with the aforementioned analysis, the PSDs show that abundant harmonic components occur at integer multiples of 20 Hz. For a low carrier frequency, i.e., 2 GHz, the sidebands decrease significantly with the increase in the harmonics. However, under the same degree

of vibration, increasing the carrier frequency, e.g., to 28 GHz, results in a large amount of power being transferred to the harmonic components due to the shorter wavelength.

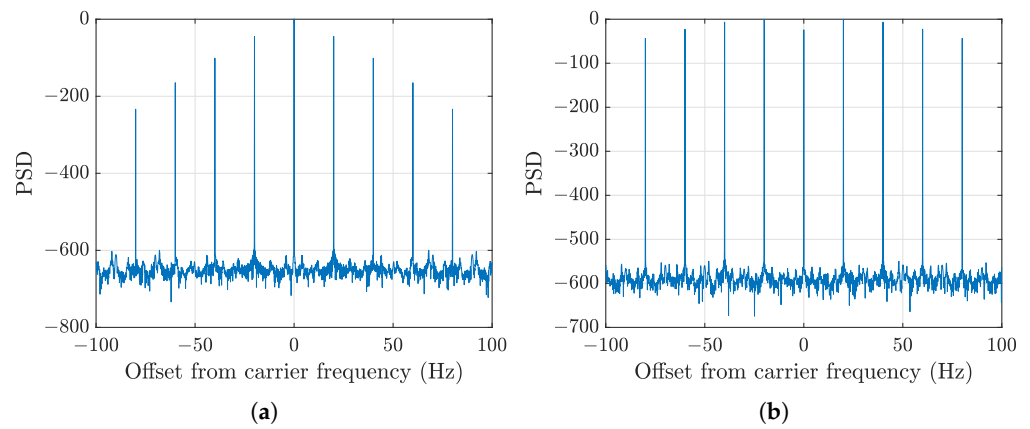


**Figure 2.** PSDs of the LoS path with (a)  $f_c = 2$  GHz, and (b)  $f_c = 28$  GHz ( $v_t = v_r = 0$  m/s,  $f_t = f_r = 20$  Hz,  $a_t = a_r = 0.01$  m,  $\gamma_t^L = \gamma_r^L = 0$ ).

In (19), the power of the LoS ray is calculated as

$$P_L = \left( \frac{\lambda}{4\pi} \right)^2 d_L^{-\gamma} G_t G_r \quad (26)$$

where  $G_t$  and  $G_r$  are the Tx and Rx antenna gains, respectively, and  $\gamma$  accounts for the path-loss exponent [16].

## 2.2. Specular and Diffuse Components

The channel matrix for the NLoS components is given as

$$\mathbf{h}_{\text{NLoS}}(t, \tau) = \mathbf{v}_r(\vartheta_n, \varphi_n) \mathbf{v}_t^H(\theta_n, \phi_n) \cdot \sum_{n=0}^N \sqrt{P_n} e^{-j\frac{2\pi}{\lambda} d_n(t)} e^{j\zeta_n} \delta(\tau - \tau_n(t)) \quad (27)$$

where  $\theta_n$ ,  $\vartheta_n$ ,  $\phi_n$ , and  $\varphi_n$  denote the ZoD, ZoA, AoD, and AoA of the  $n$ th ray, respectively. For the sake of conciseness, the subscript  $n = 0$  indicates the specular ray, and  $n = 1, \dots, N$  refers to the diffuse rays. Furthermore,  $d_n(t)$  and  $\tau_n(t) = d_n(t)/c$  are the time-varying length and delay of the  $n$ th ray, respectively. The phase shift  $\zeta_n$  is caused by the interaction of the  $n$ th wave with the ground and is obtained as  $\zeta_n = \arg(\Gamma_n)$ , where  $\arg(\cdot)$  returns the angle of a complex number and  $\Gamma_n$  is the complex reflection coefficient [37]. The modeling details of the above-mentioned parameters are described in the rest of this paper.

### 2.2.1. Lengths and Angles of the Rays

The parameters of the specular ray are calculated deterministically. However, the diffuse rays are modeled in a stochastic manner. Channel measurements reveal that the properties of the specular and diffuse components are correlated in both delay and angular domains [38]. In general, the diffuse components are distributed around the specular component. Additionally, it has been shown that scatterers are not uniformly distributed. The scatterer density gradually decreases as the distance from the center of the scattering region increases [25,39]. Based on the above-mentioned facts, the Gaussian scatter density model (GSDM) is adopted, which has been validated for modeling scatterer distribution in diverse communication scenarios [40,41]. The GSDM is expressed as

$$p_{XY}(x, y) = \frac{\exp\left(-\frac{(x-x_0)^2}{2\sigma_x^2} - \frac{y^2}{2\sigma_y^2}\right)}{2\pi\sigma_x\sigma_y} \quad (28)$$

where  $x_0 = -h_t \tan(\theta_0)$  is the distance from the specular point to  $O$  and  $\theta_0$  is the ZoD of the specular ray, which is calculated as

$$\theta_0 = \frac{\pi}{2} + \arctan\left(\frac{h_t + h_r}{D}\right). \tag{29}$$

Additionally,  $\sigma_x$  and  $\sigma_y$  control the spread of scatterers along the directions of the  $x$  and  $y$  axes, respectively. The ZoA of the specular ray is  $\vartheta_0 = \theta_0$  according to Snell's Law.

Note that (28) cannot provide any angular information. Using the Jacobian of the transformation, the joint probability density function (PDF) of the ZoDs and AoDs can be expressed as

$$p_{\Theta\Phi}(\theta, \phi) = |J(x, y)| \cdot p_{XY}(x, y) \tag{30}$$

where

$$J(x, y) = \begin{vmatrix} \frac{\partial x}{\partial \theta} & \frac{\partial x}{\partial \phi} \\ \frac{\partial y}{\partial \theta} & \frac{\partial y}{\partial \phi} \end{vmatrix} = \frac{h_t^2 \tan \theta}{\cos^2(\theta)} \tag{31}$$

$$x = -h_t \tan \theta \cos \phi \tag{32}$$

$$y = -h_t \tan \theta \sin \phi. \tag{33}$$

By substituting (28) and (31) into (30) and after several mathematical manipulations, the joint PDF of the ZoDs and AoDs is written as

$$p_{\Theta\Phi}(\theta, \phi) = \frac{-h_t^2 \tan(\theta)}{2\pi \cos^2(\theta) \sigma_x \sigma_y} \cdot \exp\left(-\frac{[h_t \tan(\theta) \cos(\phi) + x_0]^2}{2\sigma_x^2} - \frac{[h_t \tan(\theta) \sin(\phi)]^2}{2\sigma_y^2}\right) \tag{34}$$

where  $\theta \in [\pi/2, \pi]$ ,  $\phi \in [-\pi, \pi]$ . Note that this differs from previous works, such as [3,42,43], in which the scatterers are evenly distributed with a clear boundary.

Figure 3 presents the marginal PDFs of the ZoD and AoD of the diffuse rays. Three cases were used for testing. In Case I, the following parameters were chosen:  $h_t = h_r = 25$  m and  $D = 50$  m. In Case II, the height of the transmit UAV was reduced to 20 m, while the other parameters remained unchanged. In Case III, the horizontal distance between the Tx and Rx was increased, with the parameters set as  $h_t = h_r = 25$  m and  $D = 70$  m. In all three cases, the scatterer dispersion parameters were set as  $\sigma_x = 8$  and  $\sigma_y = 6$ .

Compared to Case I, a lower altitude of the Tx in Case II yields smaller ZoDs. Additionally, as the altitude of the Tx decreases, the scattering region moves closer to the Tx side, causing a larger spread of the AoDs. In Case III, the horizontal distance between the Tx and Rx increases. The larger distances from the Tx to the scatterers result in more concentrated distributions of the ZoDs and AoDs.

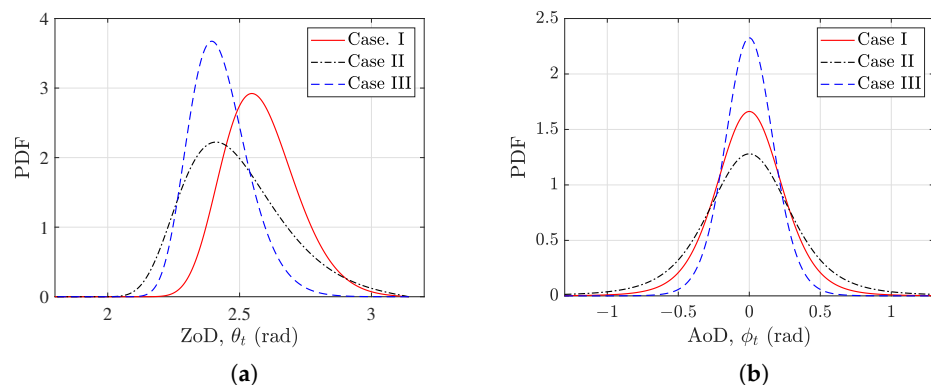


**Figure 3.** Marginal PDFs of ZoD and AoD of diffuse rays (Case I:  $h_t = h_r = 25$  m,  $D = 50$  m; Case II:  $h_t = 20$  m,  $h_r = 25$  m,  $D = 50$  m; Case III:  $h_t = h_r = 25$  m,  $D = 70$  m). (a) ZoD diffuse rays; (b) AoD diffuse rays.

For the single-bounce propagation, the arrival and departure angles are interrelated as follows:

$$\varphi_n = \begin{cases} -\pi - \arcsin\left(\frac{\sin(\phi_n)\tilde{d}_{1,n}}{\tilde{d}_{2,n}}\right), & 0 > \phi_n \geq -\pi \\ \pi - \arcsin\left(\frac{\sin(\phi_n)\tilde{d}_{1,n}}{\tilde{d}_{2,n}}\right), & \pi > \phi_n \geq 0 \end{cases} \quad (35)$$

$$\vartheta_n = \frac{\pi}{2} + \arctan\left(\frac{h_r}{\tilde{d}_{2,n}}\right) \quad (36)$$

where  $n = 1, \dots, N$ . The horizontal distances between the  $n$ th scatterer and the Tx and Rx array centers are obtained as

$$\tilde{d}_{1,n} = -h_t \tan(\theta_n) \quad (37)$$

$$\tilde{d}_{2,n} = \sqrt{\tilde{d}_{1,n}^2 + D^2 - 2\tilde{d}_{1,n}D \cos(\phi_n)}. \quad (38)$$

**Proposition 2.** *The time-varying travel distance between the Tx and Rx via the  $n$ th ray, incorporating the effects of UAV movements and antenna vibrations, can be calculated as*

$$d_n(t) \approx d_n - v_r t \sin \vartheta_n \cos \alpha_r - v_t t \sin \theta_n \cos \alpha_t - a_r \sin(2\pi f_r t) \cos \gamma_r^{(n)} - a_t \sin(2\pi f_t t) \cos \gamma_t^{(n)} \quad (39)$$

where  $\gamma_t^{(n)}$  is the angle between  $\mathbf{a}_t$  and the departure direction of the  $n$ th ray and  $\gamma_r^{(n)}$  is the angle between  $\mathbf{a}_r$  and the arrival direction of the  $n$ th ray. These angles are determined as follows:

$$\cos \gamma_t^{(n)} = \frac{\mathbf{a}_t^T \boldsymbol{\Phi}_n}{|\mathbf{a}_t| \cdot |\boldsymbol{\Phi}_n|} \quad (40)$$

$$\cos \gamma_r^{(n)} = \frac{\mathbf{a}_r^T \boldsymbol{\Psi}_n}{|\mathbf{a}_r| \cdot |\boldsymbol{\Psi}_n|} \quad (41)$$

where  $\boldsymbol{\Phi}_n$  and  $\boldsymbol{\Psi}_n$  are the departure and arrival angle unit vectors of the  $n$ th ray. Additionally,  $d_n$  is the travel distance at the initial time instant. For the specular ray, the travel distance is calculated as

$$d_0 = \sqrt{(h_t + h_r)^2 + D^2}. \quad (42)$$

Furthermore, the travel distance of the  $n$ th diffuse ray is calculated as

$$d_n = \frac{-h_t}{\cos(\theta_n)} + \frac{-h_r}{\cos(\vartheta_n)} \quad (43)$$

where  $n = 1, \dots, N$ .

The proof of (39) follows a similar procedure to the proof of (10) and is omitted for brevity.

By substituting (39) into (27), the CIR of the NLoS components of the A2A model between  $A_p^t$  and  $A_q^r$  is expressed as

$$h_{qp}^{\text{NLoS}}(t, \tau) = \sum_{n=0}^N \sqrt{P_n} \cdot e^{-j\frac{2\pi}{\lambda} d_n} \cdot e^{j\epsilon_n} \cdot e^{j2\pi(v_t^{(n)} + v_r^{(n)})t} \times e^{j\frac{2\pi}{\lambda}(p-1)\delta_t \sin \theta_n \cos(\phi_n - \xi_t)} \cdot e^{-j\frac{2\pi}{\lambda}(q-1)\delta_r \sin \theta_n \cos(\phi_n - \xi_r)} \times e^{j\frac{2\pi}{\lambda} a_t \sin(2\pi f_t t) \cos \gamma_t^{(n)}} \cdot e^{j\frac{2\pi}{\lambda} a_r \sin(2\pi f_r t) \cos \gamma_r^{(n)}} \cdot \delta(\tau - \tau_n(t)) \quad (44)$$

where  $\nu_r^{(n)}$  and  $\nu_t^{(n)}$  are the Doppler frequencies associated with the  $n$ th ray due to the motions of the Tx and Rx, respectively, which are given as

$$\nu_t^{(n)} = \frac{v_t}{\lambda} \sin \theta_n \cos(\alpha_t - \phi_n) \tag{45}$$

$$\nu_r^{(n)} = \frac{v_r}{\lambda} \sin \theta_n \cos(\alpha_r - \phi_n). \tag{46}$$

It can be observed from (44) that the time variation in the NLoS components results from the UAV movements and antenna vibrations at both ends of the link.

### 2.2.2. Powers of the Rays

The complex reflection coefficient of the  $n$ th ray is calculated according to the Fresnel law as follows [37]:

$$\Gamma_n = \frac{\cos \theta_{i,n} - Z}{\cos \theta_{i,n} + Z}. \tag{47}$$

Here,  $Z$  is expressed as  $Z_v$  and  $Z_h$  for the vertical and horizontal polarizations, respectively, i.e.,

$$Z_v = \frac{1}{\eta} \sqrt{\eta - (\sin \theta_{i,n})^2} \tag{48}$$

$$Z_h = \sqrt{\eta - (\sin \theta_{i,n})^2} \tag{49}$$

where  $\eta$  is the relative permittivity of the reflection material and  $\theta_{i,n}$  accounts for the incident angle of the  $n$ th ray and is obtained as  $\theta_{i,n} = \pi - \theta_n$ .

It is important to note that (47) holds true only for smooth surfaces. In the case of a rough surface, the incident wave splits into a specular reflected ray and multiple diffuse rays scattered in various directions, as depicted in Figure 4. Here, a scattering loss factor is introduced to account for the power attenuation via specular reflections due to the scattering effect, as follows [32]:

$$\rho_{s,n} = \exp\left(-8\pi^2 \left(\frac{\sigma_h}{\lambda}\right)^2 \cos^2(\theta_{i,n})\right) \tag{50}$$

where  $\sigma_h$  is the standard deviation of the Gaussian-distributed surface heights. Thus, the modified reflection coefficient is obtained as

$$\Gamma_{\text{mod},n} = \rho_{s,n} \Gamma_n. \tag{51}$$

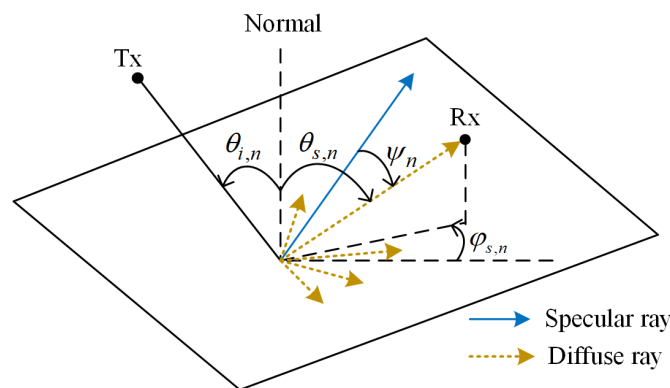


**Figure 4.** Geometry of specular reflection and diffuse scattering.

Therefore, the power of the specular ray can be calculated as

$$P_0 = PL_0^{-1} G_t G_r |\Gamma_{\text{mod},0}|^2 \tag{52}$$

where  $PL_0$  is the path loss applied to the specular ray, i.e.,

$$PL_0^{-1} = \left(\frac{\lambda}{4\pi}\right)^2 d_0^{-\gamma}. \tag{53}$$

It can be observed that by reducing the wavelength or the incident angle of the wave or by increasing the roughness of the surface, more energy will be scattered rather than reflected. The power of the  $n$ th ( $n = 1, \dots, N$ ) diffuse ray is calculated as

$$P_n = S_n^2 PL_n^{-1} G_t G_r |\Gamma_{\text{mod},n}|^2 [S_0 f(\psi_n)]^2 \tag{54}$$

where  $PL_n$  stands for the path for the  $n$ th diffuse ray, which is determined as

$$PL_n^{-1} = \left(\frac{\lambda}{4\pi}\right)^2 d_n^{-\gamma}. \tag{55}$$

Furthermore,  $S_n^2$  is the proportion of the power scattered in all directions with respect to the reflected power. Note that both  $\rho_{s,n}$  and  $S_n$  fall within the range of  $[0, 1]$ . Due to energy conservation, the total energy of the incident wave must be conserved after scattering, which means that the sum of the energies of the specular reflected and diffuse scattered waves is equal to the energy of the incident wave. Thus,  $\rho_{s,n}$  and  $S_n$  must satisfy the following constraint:

$$\rho_{s,n}^2 + S_n^2 = 1. \tag{56}$$

In (54),  $f(\psi_n)$  describes the relative power of the diffuse rays with respect to the specular direction and can be modeled by a single-lobe directive model as follows [22]:

$$f(\psi_n) = \left(\frac{1 + \cos(\psi_n)}{2}\right)^{\frac{\alpha_R}{2}} \tag{57}$$

with

$$S_0^2 = 1 / \int_0^{2\pi} \int_0^{\frac{\pi}{2}} f(\psi)^2 \sin \theta_s d\theta_s d\varphi_s. \tag{58}$$

As shown in Figure 4,  $\psi_n$  is the angle between the  $n$ th diffuse ray and the specular reflected ray originating from the same reflection point, and  $\theta_s$  and  $\varphi_s$  are the zenith and azimuth angles of the diffuse rays, respectively. The parameter  $\alpha_R$  governs the width of the scattering lobe. Based on measurements, a typical value for  $\alpha_R$  ranges from 1 to 5 [22,44,45]. To further illustrate this, Figure 5 shows the polar representation of the normalized scattering radiation pattern for an incident angle of  $\pi/4$ . It is evident that the scattering radiation pattern achieves its maximum value in the specular direction. A larger value of  $\alpha_R$  leads to a narrower scattering lobe, which means more scattered energy is concentrated around the specular reflection direction. Conversely, a smaller value of  $\alpha_R$  leads to a wider scattering lobe.

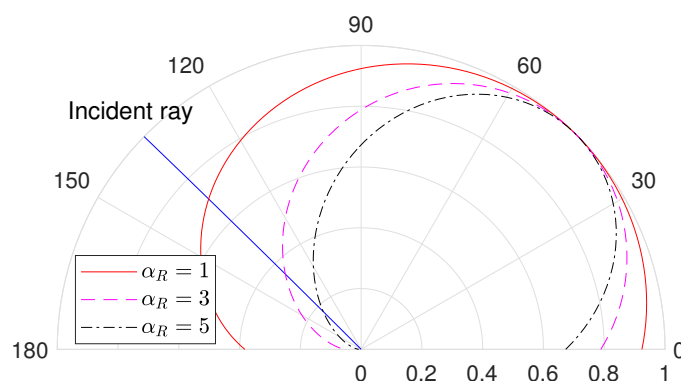


Figure 5. Polar representation of the normalized scattering radiation pattern.

In summary, the characteristics of the channel are determined by the phases and powers of MPCs, including the LoS, specular, and diffuse components. As discussed in Section 2.1, the phase of the LoS component from  $A_p^t$  to  $A_q^r$  depends on the initial distance of the LoS ray, the relative locations of  $A_p^t$  and  $A_q^r$  in the Tx and Rx arrays, and the Doppler shifts caused by the UAV flight and vibrations. Apart from the above-mentioned factors, the phases of the specular and diffuse components are also influenced by the phase shift of the reflection coefficient, i.e.,  $\zeta_n = \arg(\Gamma_n)$ . Regarding the power of the MPCs, all the MPCs experience path losses. Additionally, the energy of a wave reflected from a rough surface undergoes attenuation since a portion of the energy scatters in various directions. The attenuation of power due to reflection is quantified using (51), which depends on a combination of factors, including the carrier frequency, incident angle of the ray, and electrical properties and roughness of the reflecting materials. The proportion of scattering power is calculated using (56). Furthermore, the power of the  $n$ th diffuse component relative to the specular ray is characterized using the directive model, as demonstrated in (57).

### 3. Spatial and Temporal Correlation Characteristics

For a wideband channel, the channel transfer function is derived by performing Fourier transformation to  $h_{qp}(t, \tau)$ , i.e.,

$$H_{qp}(t, f) = \int_{-\infty}^{\infty} h_{qp}(t, \tau) e^{-j2\pi f \tau} d\tau. \quad (59)$$

The spatial-temporal CCF between  $H_{qp}(t, f)$  and  $H_{\bar{q}\bar{p}}(t - \Delta t, f)$  is defined as [35]

$$R_{qp, \bar{q}\bar{p}}(t, \Delta t) = \mathbb{E}\{H_{qp}(t, f) H_{\bar{q}\bar{p}}^*(t - \Delta t, f)\} \quad (60)$$

where  $(\cdot)^*$  is the conjugate operation and  $\mathbb{E}(\cdot)$  stands for the expectation operation. Based on (5), the spatial-temporal CCF can be expressed as the summation of the LoS and NLoS components, i.e.,

$$R_{qp, \bar{q}\bar{p}}(t, \Delta t) = R_{qp, \bar{q}\bar{p}}^{\text{LoS}}(t, \Delta t) + R_{qp, \bar{q}\bar{p}}^{\text{NLoS}}(t, \Delta t). \quad (61)$$

The channel transfer function of the LoS component can be obtained by substituting (19) into (59), i.e.,

$$\begin{aligned} H_{qp}^{\text{LoS}}(t, f) &= \sqrt{P_L} \cdot e^{-j\frac{2\pi}{\lambda} d_L} \cdot e^{j\frac{2\pi}{\lambda} (p-1)\delta_t \sin \theta_L \cos(\phi_L - \zeta_t)} \\ &\times e^{-j\frac{2\pi}{\lambda} (q-1)\delta_r \sin \theta_L \cos(\phi_L - \zeta_r)} \cdot e^{j\frac{2\pi}{\lambda} a_t \sin(2\pi f t) \cos(\gamma_t^L)} \\ &\times e^{-j\frac{2\pi}{\lambda} a_r \sin(2\pi f t) \cos(\gamma_r^L)} \cdot e^{j2\pi(v_t^L + v_r^L)t} \cdot e^{-j2\pi \tau_L(t) f}. \end{aligned} \quad (62)$$

By substituting  $H_{qp}^{\text{LoS}}(t, f)$  and  $H_{\bar{q}\bar{p}}^{\text{LoS}}(t - \Delta t, f)$  into (60), the spatial-temporal CCF of the LoS component is given as

$$\begin{aligned} R_{qp, \bar{q}\bar{p}}^{\text{LoS}}(t, \Delta t) &= \mathbb{E}\{P_L \cdot e^{j2\pi(v_t + v_r)\Delta t} \cdot e^{j2\pi f[\tau_n(t - \Delta t) - \tau_n(t)]} \\ &\times e^{j\frac{2\pi}{\lambda} [\Delta d_t \sin(\theta_L) \cos(\zeta_t) + \Delta d_r \sin(\theta_L) \cos(\zeta_r)]} \\ &\times e^{j\frac{2\pi}{\lambda} a_r [\sin(2\pi f t) - \sin(2\pi f (t - \Delta t))] \cos \gamma_r^L} \\ &\times e^{-j\frac{2\pi}{\lambda} a_t [\sin(2\pi f t) - \sin(2\pi f (t - \Delta t))] \cos \gamma_t^L} \} \end{aligned} \quad (63)$$

where  $\Delta d_t = (p - \bar{p})\delta_t$  is the spacing between  $A_p^T$  and  $A_{\bar{p}}^T$ ,  $\Delta d_r = (q - \bar{q})\delta_r$  accounts for the spacing between  $A_q^R$  and  $A_{\bar{q}}^R$ , and  $a_t \sim U(-a_{tm}, a_{tm})$ ,  $a_r \sim U(-a_{rm}, a_{rm})$ . By applying the equality  $\mathbb{E}\{e^{jtx}\} = \frac{e^{jtb} - e^{jta}}{jt(b-a)}$ , where  $x \sim U(a, b)$ , we have

$$\begin{aligned}
 & R_{qp, \bar{q}\bar{p}}^{\text{LoS}}(t, \Delta t) \\
 &= P_L \cdot e^{j2\pi(v_t + v_r)\Delta t} \cdot e^{j2\pi f[\tau_n(t - \Delta t) - \tau_n(t)]} \\
 &\times e^{j\frac{2\pi}{\lambda}[\Delta d_t \sin(\theta_L) \cos(\xi_t) + \Delta d_r \sin(\theta_L) \cos(\xi_r)]} \\
 &\times \frac{\sin\left(\frac{2\pi}{\lambda} a_{tm} [\sin(2\pi f_t t) - \sin(2\pi f_t(t - \Delta t))]\right) \cos \gamma_t^L}{\frac{2\pi}{\lambda} a_{tm} [\sin(2\pi f_t t) - \sin(2\pi f_t(t - \Delta t))] \cos \gamma_t^L} \\
 &\times \frac{\sin\left(\frac{2\pi}{\lambda} a_{rm} [\sin(2\pi f_r(t - \Delta t)) - \sin(2\pi f_r t)]\right) \cos \gamma_r^L}{\frac{2\pi}{\lambda} a_{rm} [\sin(2\pi f_r(t - \Delta t)) - \sin(2\pi f_r t)] \cos \gamma_r^L}. \tag{64}
 \end{aligned}$$

Based on the definition of the sinc function, i.e.,  $\text{sinc}(x) = \frac{\sin(\pi x)}{\pi x}$ , the spatial-temporal CCF of the LoS component is further written as

$$\begin{aligned}
 & R_{qp, \bar{q}\bar{p}}^{\text{LoS}}(t, \Delta t) \\
 &= P_L \cdot e^{j2\pi(v_t + v_r)\Delta t} \cdot e^{j2\pi f[\tau_n(t - \Delta t) - \tau_n(t)]} \\
 &\times e^{j\frac{2\pi}{\lambda}[\Delta d_t \sin(\theta_L) \cos(\xi_t) + \Delta d_r \sin(\theta_L) \cos(\xi_r)]} \\
 &\times \text{sinc}\left(\frac{2}{\lambda} [\sin(2\pi f_t t) - \sin(2\pi f_t(t - \Delta t))] \cos \gamma_t^L a_{tm}\right) \\
 &\times \text{sinc}\left(\frac{2}{\lambda} [\sin(2\pi f_r(t - \Delta t)) - \sin(2\pi f_r t)] \cos \gamma_r^L a_{rm}\right). \tag{65}
 \end{aligned}$$

Employing a similar procedure, the spatial-temporal CCF of the NLoS component can be expressed as

$$\begin{aligned}
 & R_{qp, \bar{q}\bar{p}}^{\text{NLoS}}(t, \Delta t) \\
 &= \mathbb{E}\left\{ \sum_{n=0}^N P_n \cdot e^{j2\pi(v_t^{(n)} + v_r^{(n)})\Delta t} \cdot e^{j2\pi f[\tau_n(t - \Delta t) - \tau_n(t)]} \right. \\
 &\times e^{j\frac{2\pi}{\lambda}[\Delta d_t \sin(\theta_n) \cos(\xi_t - \phi_n) - \Delta d_r \sin(\theta_n) \cos(\xi_r - \phi_n)]} \\
 &\times \text{sinc}\left(\frac{2}{\lambda} [\sin(2\pi f_t t) - \sin(2\pi f_t(t - \Delta t))] \cos \gamma_t^{(n)} a_{tm}\right) \\
 &\left. \times \text{sinc}\left(\frac{2}{\lambda} [\sin(2\pi f_r t) - \sin(2\pi f_r(t - \Delta t))] \cos \gamma_r^{(n)} a_{rm}\right) \right\}. \tag{66}
 \end{aligned}$$

The spatial-temporal CCF plays a key role in channel characteristic analysis since it is the foundation for deriving many other channel statistics. For example, by setting  $\bar{p} = p$  and  $\bar{q} = q$ , (61) reduces to the temporal autocorrelation function (ACF), i.e.,  $R_{qp}(t, \Delta t)$ . By setting  $\Delta t = 0$ , (61) reduces to the spatial CCF, i.e.,  $R_{qp, \bar{q}\bar{p}}(t)$ . By setting  $a_{tm} = a_{rm} = 0$ , (61) reduces to the spatial-temporal CCF, neglecting the UAV vibrations.

Additionally, the Doppler PSD depicts how the channel power is distributed across the Doppler frequency and can be calculated as the Fourier transform of the temporal ACF in terms of  $\Delta t$ , i.e.,

$$S_{qp}(t, \nu) = \int_{-\infty}^{\infty} R_{qp}(t, \Delta t) e^{-j2\pi \Delta t \cdot \nu} d\Delta t. \tag{67}$$

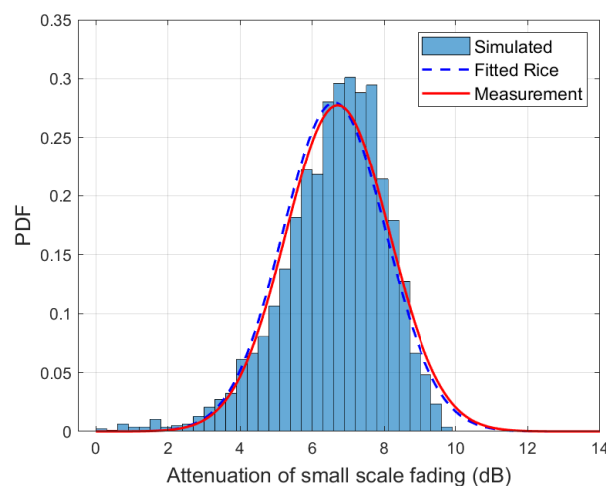
In addition, the coherence time is the duration over which the channel stays almost constant and can be defined as the minimum time interval in which the normalized temporal ACF is below a certain threshold  $c$ , expressed as [46]

$$T_c = \min \left\{ \Delta t : \frac{|R_{qp}(t, \Delta t)|}{\max\{|R_{qp}(t, \Delta t)|\}} \leq c \right\}. \quad (68)$$

#### 4. Results and Analysis

This section presents the results of the proposed channel model. Unless otherwise stated, the basic parameters are chosen as follows:  $D = 50$  m,  $h_t = h_r = 25$  m,  $G_t = G_r = 5$  dBi [47],  $\gamma = 2$ ,  $\eta = 3$  [48],  $\sigma_h = 0.02$  m [49],  $\alpha_R = 1$  [22],  $\delta_t = \delta_r = \lambda/2$ ,  $\zeta_t = \zeta_r = \pi/2$ ,  $N = 1000$ ,  $\sigma_x = 5.93$  m,  $\sigma_y = 4.81$  m,  $v_t = v_r = 10$  m/s, and  $\alpha_t = \alpha_r = 0$ . Additionally, the maximum vibration amplitude is  $a_{tm} = a_{rm} = 0.01$  m, the vibration frequency is set as  $f_t = f_r = 24$  Hz (120 rpm/V, 12 V) [50], and the vibration directions are defined by the azimuth angles,  $\zeta_t^A = \zeta_r^A = \pi/6$ , and elevation angles,  $\zeta_t^E = \zeta_r^E = \pi/10$ . Furthermore, vertical polarization antennas are assumed in the simulation. Note that the parameters, including the carrier frequency, UAV altitudes, Tx–Rx separation, and antenna gain, are established in accordance with the measurement campaign in [47]. Only a limited set of parameters, such as  $\sigma_x$  and  $\sigma_y$ , which distinguish the proposed model from conventional ones, are derived through the fitting of the statistical properties of the model to the measurement data.

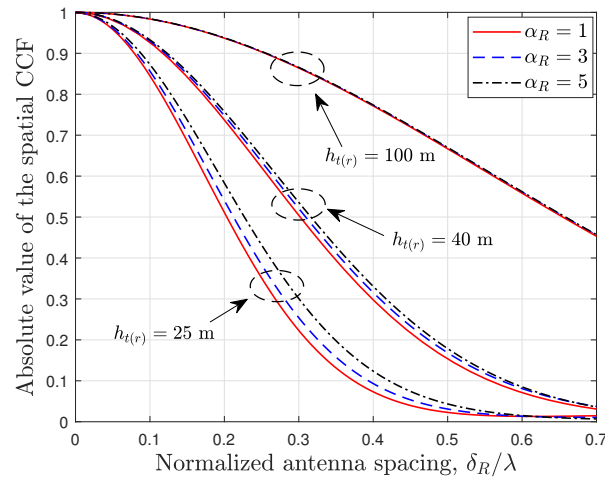
Figure 6 shows the PDF of the attenuation of small-scale fading of the proposed model and the measurement results in [47]. The A2A measurements were conducted at 2.4 GHz using Wistron DNMA92 and TP-Link WN821N adapters, following [51]. Two AscTec Firefly UAVs equipped with omnidirectional antennas with a 5 dBi gain were used, and the transmission power was set at 20 dBm. During the measurements, the UAVs maintained a horizontal separation of 50 m and operated at an altitude of 25 m. The received signal strength values were recorded and analyzed. In the simulation, model parameters such as the carrier frequency, Tx–Rx separation, antenna gain, and UAV height were set according to the measurement campaign in [47]. The scatterer density parameters, i.e.,  $\sigma_x$  and  $\sigma_y$ , were obtained by fitting the statistics to the measurement results. Due to the impacts of the LoS and ground reflection paths, the proposed model illustrates typical Rice fading [47]. The agreement between the simulation and measurement results demonstrates the practicability of the model.



**Figure 6.** PDF of attenuation of small-scale fading of the proposed model and measurement results in [47] ( $f_c = 2.4$  GHz,  $D = 50$  m,  $h_t = h_r = 25$  m,  $\sigma_x = 5.93$  m,  $\sigma_y = 4.81$  m).

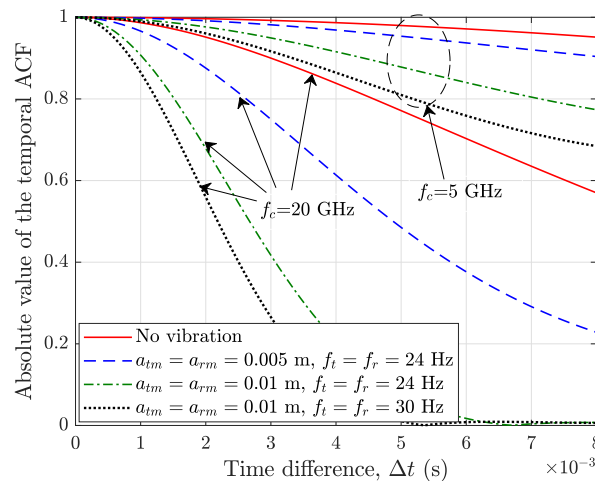
Figure 7 illustrates the spatial CCFs of the proposed model with different UAV heights and scattering-lobe widths. It is found that a large  $\alpha_R$ , which results in narrower scattering lobes, increases the spatial CCFs of the model. This implies that an environment with

less scattering can increase the spatial correlation of the channel, thereby decreasing the spatial diversity of a MIMO system. Additionally, as the UAV height increases, the spatial correlation becomes higher due to the smaller angular spread. With the same horizontal distance between the Tx and Rx, a greater UAV height of 100 m results in increased path loss for the diffuse rays. Consequently, the A2A channel is primarily dominated by the LoS ray. As a result, the influence of the scattering-lobe widths on the spatial CCF becomes negligible.



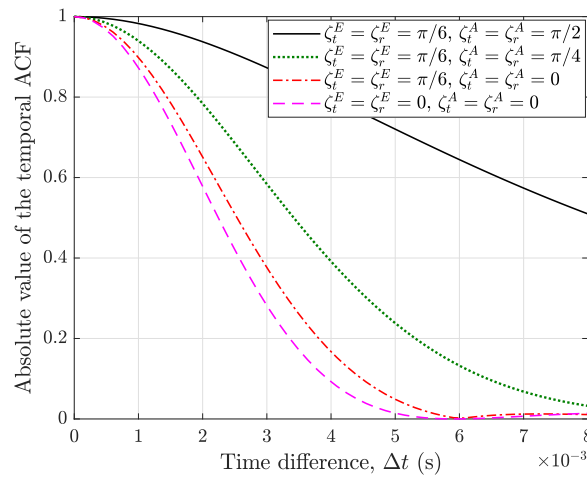
**Figure 7.** The spatial CCFs of the proposed A2A channel model with different UAV heights and scattering-lobe widths ( $f_c = 2.4$  GHz).

Figure 8 shows the temporal ACFs of the proposed A2A channel model with different vibration amplitudes, vibration frequencies, and carrier frequencies. It can be observed that an increasing vibration amplitude or vibration frequency results in a lower temporal correlation of the channel, implying a faster time variation in the channel over time. A noteworthy insight observed from the results is that the temporal ACF demonstrates a high sensitivity to UAV vibrations when the system operates at high-frequency bands. A higher carrier frequency makes the channel decorrelate over time more rapidly. The underlying reason for this is that the antenna vibration induces a larger phase rotation of the wave with a shorter wavelength, leading to a rapidly time-varying channel and a lower temporal ACF. This result aligns with the theoretical analysis in (23), which indicates that a higher carrier frequency or a shorter wavelength results in a larger Doppler frequency caused by the antenna vibration, leading to a rapid decorrelation of the channel over time.



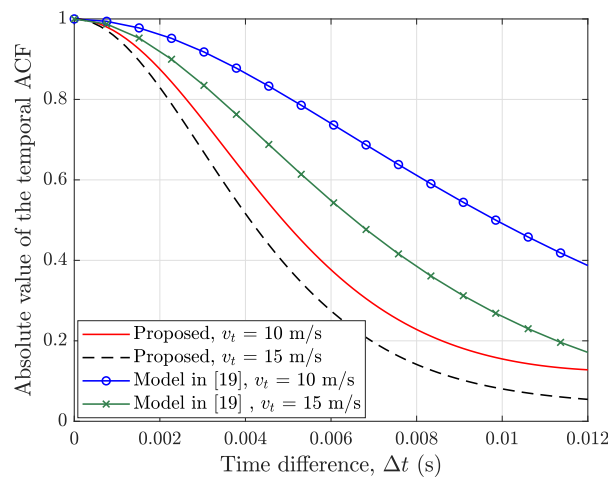
**Figure 8.** The temporal ACFs of the proposed A2A channel model with different vibration amplitudes, vibration frequencies, and carrier frequencies.

Figure 9 illustrates the impact of UAV vibration angles on the temporal ACFs of the proposed model. The analysis reveals that the strongest temporal correlation occurs when the UAVs vibrate perpendicular to the line connecting the Tx and Rx. As the vibration azimuth angle decreases, the temporal ACF gradually reduces. Moreover, the temporal ACF further reduces by decreasing the vibration elevation angle. Note that in the case of rotary-wing UAVs, vibration is mainly caused by the imbalance in the rotor blades, leading to predominantly horizontal vibrations. This can cause a significant decrease in the temporal ACF and result in rapid temporal variations in the channel.



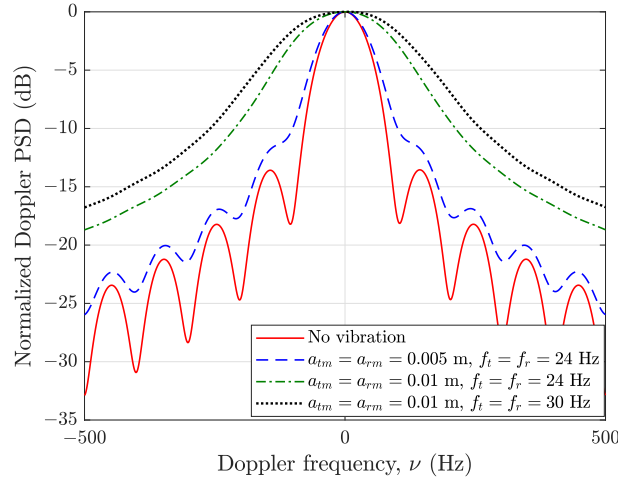
**Figure 9.** The temporal ACFs of the proposed A2A channel model with different vibration angles of the UAV ( $f_c = 20$  GHz,  $f_t = f_r = 24$  GHz).

Figure 10 compares the proposed model with the model in [19] regarding the temporal ACF at different speeds of the transmit UAV. The A2A channel model in [19] employs a geometric method with a scattering region defined as an ellipsoid truncated by the ground plane, with the Tx and Rx positioned as the focal points. To ensure a fair comparison, both models were assessed under the same experimental conditions, including the carrier frequency, Tx–Rx distance, UAV heights, movement directions, and speeds. The results demonstrate that the temporal ACFs of both models diminish as the UAV speed increases. Furthermore, the model in [19] fails to consider the impacts of UAV vibration and significant ground reflections, resulting in higher temporal correlations than those observed in the proposed model.



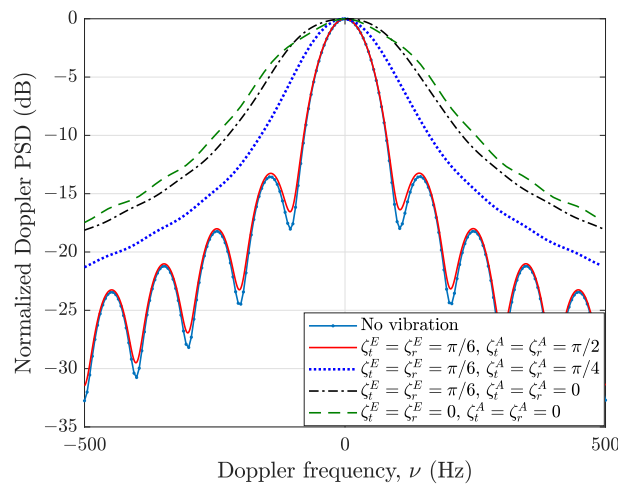
**Figure 10.** Comparison of the proposed A2A channel model and the model in [19] in terms of temporal ACF for different speeds of the transmit UAV ( $f_c = 20$  GHz,  $f_t = f_r = 24$  GHz,  $a_{tm} = a_{rm} = 0.005$  m,  $D = 50$  m,  $h_t = h_r = 25$  m).

Figure 11 shows the Doppler PSDs of the proposed A2A channel model with different degrees of UAV vibrations. With the amplification of the vibration amplitude, the Doppler PSD demonstrates a more extensive dispersion across the Doppler frequency axis, indicating an abundance of Doppler frequency components. Similarly, as the vibration frequency increases, the Doppler PSD spreads more extensively. This finding aligns with the theoretical results in (23), indicating that UAV vibrations bring in extra Doppler frequencies, which are influenced by both the vibration amplitudes and frequencies.



**Figure 11.** The Doppler PSDs of the proposed A2A channel model with different degrees of UAV vibrations ( $f_c = 20$  GHz).

Figure 12 illustrates the effects of the vibration angles on the Doppler PSD of the model. It is shown that when the UAVs vibrate perpendicular to the line connecting the Tx and Rx, the influence on the Doppler PSD is negligible. The impact of UAV vibration becomes more pronounced as the vibration azimuth angle decreases. A smaller vibration azimuth angle leads to a broader dispersion of the Doppler PSD across the Doppler frequency axis. It is worth noting that when the UAVs vibrate along the LoS path, the Doppler PSD exhibits the widest range of frequency components. This observation indicates a rich variety of Doppler frequencies present in the channel.



**Figure 12.** The Doppler PSDs of the proposed A2A channel model with different UAV vibration angles ( $f_c = 20$  GHz,  $f_t = f_r = 24$  Hz,  $a_{tm} = a_{rm} = 0.01$  m).

Figure 13 shows the coherence times of the proposed model with different degrees of UAV vibrations and carrier frequencies. It can be observed that the coherence times are in the order of microseconds. Under identical vibration intensities, i.e.,  $f_t = f_r = 24$  GHz,

$a_{tm} = a_{rm} = 0.005$  m, the coherence time reduces as the carrier frequency increases. Specifically, for a given threshold, e.g.,  $c = 0.9$ ,  $T_c = \{6.81, 3.14, 1.58\}$  ms for  $f_c = \{5, 10, 20\}$  GHz, respectively. Furthermore, a larger vibration amplitude or frequency results in shorter coherence times of the channel, which means the channel experiences more rapid fluctuations. As a consequence, more frequent channel estimation is necessary to keep up with the variations in the channel, especially for systems operating at high-frequency bands.

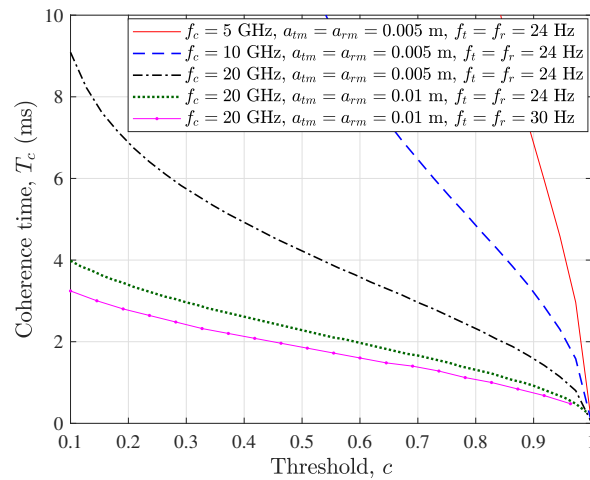


**Figure 13.** The coherence times of the proposed A2A channel model with different degrees of UAV vibrations and carrier frequencies.

## 5. Conclusions

This paper has presented a novel A2A channel model, which incorporates the propagation mechanisms of direct transmission, specular reflection, and diffuse scattering. Based on the Gaussian scatter density, a closed-form PDF that jointly describes the zenith and azimuth angles of diffuse rays has been proposed. The power of diffuse rays has been obtained considering the path loss, reflection coefficient, and scattering radiation pattern of the channel. Additionally, UAV vibrations have been considered and modeled using stochastic sinusoidal processes. The utility of the model has been validated by comparing the statistics with measurement results. Statistics including the spatial-temporal CCF, Doppler PSD, and coherence time have been obtained. The findings suggest that the scattering effect exhibits a pronounced dependence on the UAV altitudes. A large vibration amplitude or frequency significantly amplifies the Doppler spread and diminishes the temporal correlation and coherence time of the channel. For a given strength of UAV vibration, the adverse effects of UAV vibrations increase with the carrier frequency, posing a great challenge for UAV communications in high-frequency bands.

**Author Contributions:** Conceptualization, W.Q. and J.B.; methodology, W.Q. and J.B.; software, Z.W.; formal analysis, Z.W.; investigation, W.Q. and J.B.; resources, Z.W.; writing—original draft preparation, Z.W.; writing—review and editing, W.Q., J.B. and W.L.; visualization, Z.W.; supervision, W.Q. and J.B.; project administration, W.L. All authors have read and agreed to the published version of the manuscript.

**Funding:** This research was funded by the National Natural Science Foundation of China (NSFC), grant number 62101311.

**Data Availability Statement:** Data are contained within the article.

**Conflicts of Interest:** Authors Wenzhe Qi and Wenzhao Liu were employed by the State Grid Shandong Electric Power Company Zibo Power Supply Company. The remaining authors declare that the research was conducted in the absence of any commercial or financial relationships that could be construed as a potential conflict of interest.

## References

1. Wang, C.X.; You, X.; Gao, X.; Zhu, X.; Li, Z.; Zhang, C.; Wang, H.; Huang, Y.; Chen, Y.; Haas, H.; et al. On the road to 6G: Visions, requirements, key technologies, and testbeds. *IEEE Commun. Surveys Tuts.* **2023**, *25*, 905–974. [\[CrossRef\]](#)
2. Yan, C.; Fu, L.; Zhang, J.; Wang, J. A Comprehensive survey on UAV communication channel modeling. *IEEE Access* **2019**, *7*, 107769–107792. [\[CrossRef\]](#)
3. Chang, H.; Bian, J.; Wang, C.X.; Bai, Z.; Zhou, W.; Aggoune, e.H.M. A 3D non-stationary wideband GBSM for low-altitude UAV-to-ground V2V MIMO channels. *IEEE Access* **2019**, *7*, 70719–70732. [\[CrossRef\]](#)
4. Chang, H.; Wang, C.X.; Bian, J.; Feng, R.; He, Y.; Chen, Y.; Aggoune, E.H.M. A novel 3D beam domain channel model for UAV massive MIMO communications. *IEEE Trans. Wireless Commun.* **2023**, *22*, 5431–5445. [\[CrossRef\]](#)
5. Mao, K.; Zhu, Q.; Qiu, Y.; Liu, X.; Song, M.; Fan, W.; Kokkeler, A.B.J.; Miao, Y. A UAV-aided real-time channel sounder for highly dynamic nonstationary A2G scenarios. *IEEE Trans. Instrum. Meas.* **2023**, *72*, 1–15. [\[CrossRef\]](#)
6. Lian, Z.; Su, Y.; Wang, Y.; Ji, P.; Jin, B.; Zhang, Z.; Xie, Z. A novel geometry-based 3-D wideband channel model and capacity analysis for IRS-assisted UAV communication systems. *IEEE Trans. Wireless Commun.* **2023**, *22*, 5502–5517. [\[CrossRef\]](#)
7. Bian, J.; Wang, C.X.; Liu, Y.; Tian, J.; Qiao, J.; Zheng, X. 3D non-stationary wideband UAV-to-ground MIMO channel models based on aeronautic random mobility model. *IEEE Trans. Veh. Technol.* **2021**, *70*, 11154–11168. [\[CrossRef\]](#)
8. Bai, L.; Huang, Z.; Cheng, X. A non-stationary 6G UAV channel model with 3D continuously arbitrary trajectory and self-rotation. *IEEE Trans. Wireless Commun.* **2022**, *21*, 10592–10606. [\[CrossRef\]](#)
9. Hua, B.; Ni, H.; Zhu, Q.; Wang, C.X.; Zhou, T.; Mao, K.; Bao, J.; Zhang, X. Channel modeling for UAV-to-ground communications with posture variation and fuselage scattering effect. *IEEE Trans. Commun.* **2023**, *71*, 3103–3116. [\[CrossRef\]](#)
10. Ma, Z.; Ai, B.; He, R.; Wang, G.; Niu, Y.; Yang, M.; Wang, J.; Li, Y.; Zhong, Z. Impact of UAV rotation on MIMO channel characterization for air-to-ground communication systems. *IEEE Trans. Veh. Technol.* **2020**, *69*, 12418–12431. [\[CrossRef\]](#)
11. Banagar, M.; Dhillon, H.S.; Molisch, A.F. Impact of UAV wobbling on the air-to-ground wireless channel. *IEEE Trans. Veh. Technol.* **2020**, *69*, 14025–14030. [\[CrossRef\]](#)
12. Dabiri, M.T.; Rezaee, M.; Yazdani, V.; Maham, B.; Saad, W.; Hong, C.S. 3D channel characterization and performance analysis of UAV-assisted millimeter wave links. *IEEE Trans. Wireless Commun.* **2021**, *20*, 110–125. [\[CrossRef\]](#)
13. Ma, Z.; Ai, B.; He, R.; Wang, G.; Zhong, Z.; Yang, M.; Wang, J.; Li, Y. Impact of UAV rotation on MIMO channel space-time correlation. In Proceedings of the IEEE 92nd Vehicular Technology Conference (VTC2020-Fall), Victoria, BC, Canada, 18 November–16 December 2020; pp. 1–5. [\[CrossRef\]](#)
14. Al-Mashhadani, M.A. Random vibrations in unmanned aerial vehicles, mathematical analysis and control methodology based on expectation and probability. *J. Low Freq. Noise Vib. Act. Control* **2019**, *38*, 143–153. [\[CrossRef\]](#)
15. Hoffmann, F.; Ritchie, M.; Fioranelli, F.; Charlish, A.; Griffiths, H. Micro-Doppler based detection and tracking of UAVs with multistatic radar. In Proceedings of the 2016 IEEE Radar Conference (RadarConf), Philadelphia, USA, 2–6 May 2016; pp. 1–6. [\[CrossRef\]](#)
16. Liu, T.; Zhang, Z.; Jiang, H.; Qian, Y.; Liu, K.; Dang, J.; Wu, L. Measurement-based characterization and modeling for low-altitude UAV air-to-air channels. *IEEE Access* **2019**, *7*, 98832–98840. [\[CrossRef\]](#)
17. Ede, B.; Kaplan, B.; Kahraman, i.; Kesir, S.; Yarkan, S.; Ekti, A.R.; Baykaş, T.; Görçin, A.; Çırpan, H.A. Measurement-based large scale statistical modeling of air-to-air wireless UAV channels via novel time-frequency analysis. *IEEE Wireless Commun. Lett.* **2022**, *11*, 136–140. [\[CrossRef\]](#)
18. Zhou, L.; Yang, Z.; Zhao, G.; Zhou, S.; Wang, C.X. Propagation characteristics of air-to-air channels in urban environments. In Proceedings of the IEEE Global Communications (GLOBECOM), Abu Dhabi, United Arab Emirates, 9–13 December 2018; pp. 1–6. [\[CrossRef\]](#)
19. Mao, X.; Wang, C.X.; Chang, H. A 3D non-stationary geometry-based stochastic model for 6G UAV air-to-air channels. In Proceedings of the International Conference on Wireless Communications and Signal Processing (WCSP), Changsha, China, 20–22 October 2021; pp. 1–5. [\[CrossRef\]](#)
20. Zhang, Y.; Zhou, Y.; Ji, Z.; Lin, K.; He, Z. A three-dimensional geometry-based stochastic model for air-to-air UAV channels. In Proceedings of the IEEE Conference on Vehicular Technology (VTC), Victoria, BC, Canada, 18 November–16 December 2020; pp. 1–5. [\[CrossRef\]](#)
21. Ma, Z.; Ai, B.; He, R.; Wang, G.; Niu, Y.; Zhong, Z. A wideband non-stationary air-to-air channel model for UAV communications. *IEEE Trans. Veh. Technol.* **2020**, *69*, 1214–1226. [\[CrossRef\]](#)
22. Degli-Esposti, V.; Fuschini, F.; Vitucci, E.M.; Falciaesca, G. Measurement and modelling of scattering from buildings. *IEEE Trans. Antennas Propag.* **2007**, *55*, 143–153. [\[CrossRef\]](#)
23. Hanssens, B.; Kshetri, S.R.; Tanghe, E.; Plets, D.; Hoebeke, J.; Karaağaç, A.; Haxhibeqiri, J.; Gaillot, D.P.; Liénard, M.; Oestges, C.; et al. Measurement-based analysis of dense multipath components in a large industrial warehouse. In Proceedings of the European Conference on Antennas and Propagation (EuCAP), London, UK, 9–13 April 2018; pp. 1–5. [\[CrossRef\]](#)
24. Rashdan, I.; Unterhuber, P.; de Ponte Müller, F.; Sand, S.; Caire, G. Diffuse multipath analysis of vehicle-to-vulnerable road user channel in urban environment. In Proceedings of the European Conference on Antennas and Propagation (EuCAP), Dusseldorf, Germany, 22–26 March 2021; pp. 1–5. [\[CrossRef\]](#)
25. Virk, U.T.; Haneda, K.; Wagen, J.F. Dense multipath components add-on for COST 2100 channel model. In Proceedings of the European Conference on Antennas and Propagation (EuCAP), Lisbon, Portugal, 13–17 April 2015; pp. 1–5.

26. Mao, K.; Zhu, Q.; Song, M.; Li, H.; Ning, B.; Pedersen, G.F.; Fan, W. Machine-learning-based 3-D channel modeling for U2V mmWave communications. *IEEE Internet Things J.* **2022**, *9*, 17592–17607. [CrossRef]
27. Xia, W.; Rangan, S.; Mezzavilla, M.; Lozano, A.; Geraci, G.; Semkin, V.; Loianno, G. Generative neural network channel modeling for millimeter-wave UAV communication. *IEEE Trans. Wireless Commun.* **2022**, *21*, 9417–9431. [CrossRef]
28. Tian, Y.; Li, H.; Zhu, Q.; Mao, K.; Ali, F.; Chen, X.; Zhong, W. Generative network-based channel modeling and generation for air-to-ground Communication scenarios. *IEEE Commun. Lett.* **2024**, *28*, 892–896. [CrossRef]
29. Wang, J.; Zhu, Q.; Lin, Z.; Wu, Q.; Huang, Y.; Cai, X.; Zhong, W.; Zhao, Y. Sparse Bayesian learning-based 3-D radio environment map construction—Sampling optimization, scenario-dependent dictionary construction, and sparse recovery. *IEEE Trans. Cogn. Commun. Netw.* **2024**, *10*, 80–93. [CrossRef]
30. Hou, X.; Wang, J.; Jiang, C.; Zhang, X.; Ren, Y.; Debbah, M. UAV-enabled covert federated learning. *IEEE Trans. Wireless Commun.* **2023**, *22*, 6793–6809. [CrossRef]
31. Wang, Y.; Su, Z.; Zhang, N.; Benslimane, A. Learning in the air: Secure federated learning for UAV-assisted crowdsensing. *IEEE Trans. Netw. Sci. Eng.* **2021**, *8*, 1055–1069. [CrossRef]
32. Rappaport, T.S. *Wireless Communications: Principles and Practice*, 2nd ed.; Pearson Education: Upper Saddle River, NJ, USA, 2010.
33. Khuwaja, A.A.; Chen, Y.; Zhao, N.; Alouini, M.S.; Dobbins, P. A survey of channel modeling for UAV communications. *IEEE Commun. Surveys Tuts.* **2018**, *20*, 2804–2821. [CrossRef]
34. Kilgore, I.M.; Kabiri, S.A.; Kane, A.W.; Steer, M.B. The effect of chaotic vibrations on antenna characteristics. *IEEE Antennas Wireless Propag. Lett.* **2016**, *15*, 1242–1244. [CrossRef]
35. Bian, J.; Wang, C.X.; Gao, X.; You, X.; Zhang, M. A general 3D non-stationary wireless channel model for 5G and beyond. *IEEE Trans. Wireless Commun.* **2021**, *20*, 3211–3224. [CrossRef]
36. Colton, D.; Kress, R. *Inverse Acoustic and Electromagnetic Scattering Theory*, 2nd ed.; Springer: New York, NY, USA, 1998.
37. Oestges, C.; Clerckx, B. *MIMO Wireless Communications: From Real-World Propagation to Space-Time Code Design*, 1st ed.; Academic Press: London, UK, 2010.
38. Quitin, F.; Oestges, C.; Bellens, F.; van Roy, S.; Horlin, F.; De Doncker, P. Extracting specular-diffuse clusters from MIMO channel measurements. In Proceedings of the International Symposium on Personal, Indoor and Mobile Radio Communications (PIMRC), Toronto, ON, Canada, 11–14 September 2011; pp. 940–944. [CrossRef]
39. Santos, T.; Tufvesson, F.; Molisch, A.F. Modeling the ultra-wideband outdoor channel: Model specification and validation. *IEEE Trans. Wireless Commun.* **2010**, *9*, 1987–1997. [CrossRef]
40. Andrade, A.; Covarrubias, D. Radio channel spatial propagation model for mobile 3G in smart antenna systems. *IEICE Trans. Commun.* **2003**, *E86-B*, 213–220.
41. Kelner, J.M.; Ziolkowski, C. Adjustment of the gaussian scatterer density model to different mobile radio propagation environment. In Proceedings of the 10th European Conference on Antennas and Propagation (EuCAP), Davos, Switzerland, 10–15 April 2016; pp. 1–5.
42. Zaixue, W.; Qipeng, T. Analytical RS-GBSM-based nonstationary low-altitude air-to-air channel modeling over open area. *Int. J. Antennas Propag.* **2022**, *2022*, 1–18. [CrossRef]
43. Wei, Z.; Geng, J. Time-variant PDFs of AODs and AOA for ground scattering in low-altitude air-to-air communication over open area. *IEEE Commun. Lett.* **2021**, *25*, 701–705. [CrossRef]
44. Mani, F.; Quitin, F.; Oestges, C. Accuracy of depolarization and delay spread predictions using advanced ray-based modeling in indoor scenarios. *J. Wireless Com. Netw.* **2011**, *2011*, 11. [CrossRef]
45. Pascual-García, J.; Molina-García-Pardo, J.M.; Martínez-Inglés, M.T.; Rodríguez, J.V.; Saurín-Serrano, N. On the importance of diffuse scattering model parameterization in indoor wireless channels at mm-wave frequencies. *IEEE Access* **2016**, *4*, 688–701. [CrossRef]
46. Va, V.; Heath, R.W. Basic relationship between channel coherence time and beamwidth in vehicular channels. In Proceedings of the Conference on Vehicular Technology (VTC), Boston, MA, USA, 6–9 September 2015; pp. 1–5. [CrossRef]
47. Goddemeier, N.; Wietfeld, C. Investigation of air-to-air channel characteristics and a UAV specific extension to the rice model. In Proceedings of the Global Communications Conference (GLOBECOM), San Diego, CA, USA, 6–10 December 2015; pp. 1–5. [CrossRef]
48. *ITU-R P.527*; Electrical Characteristics of the Surface of the Earth. ITU-R: Geneva, Switzerland, 2021.
49. Egido, A.; Paloscia, S.; Motte, E.; Guerriero, L.; Pierdicca, N.; Caparrini, M.; Santi, E.; Fontanelli, G.; Floury, N. Airborne GNSS-R polarimetric measurements for soil moisture and above-ground biomass estimation. *IEEE J. Sel. Top. Appl. Earth Obs. Remote Sens.* **2014**, *7*, 1522–1532. [CrossRef]
50. DJI Website. Available online: <https://www.dji.com/hk-en/e5000> (accessed on 5 April 2024).
51. *IEEE Std 802.11n TM-2009*; Part 11: Wireless LAN Medium Access Control (MAC) and Physical Layer (PHY) Specifications—Amendment 5: Enhancements for Higher Throughput. IEEE 802.11 Working Group: New York, NY, USA, 2009.

**Disclaimer/Publisher’s Note:** The statements, opinions and data contained in all publications are solely those of the individual author(s) and contributor(s) and not of MDPI and/or the editor(s). MDPI and/or the editor(s) disclaim responsibility for any injury to people or property resulting from any ideas, methods, instructions or products referred to in the content.